JOURNAL OF MATERIALS SCIENCE **39** (2004) 6183–6190

'Smart' Raman/Rayleigh imaging of nanosized SiC materials using the spatial correlation model

M. HAVEL
Nanophases and Heterogeneous Solids Group, LADIR-UMR7075 Centre National de la Recherche Scientifique & Université Pierre et Marie Curie, 2 rue Henry Dunant, 94320 Thiais, France; Département des Matériaux et Systèmes Composites, Office National d'Etudes et de Recherches Aérospatiales, 29 Ave de la Division Leclerc, 92320 Chatillon, France

D. BARON, Ph. COLOMBAN*
Nanophases and Heterogeneous Solids Group, LADIR-UMR7075 Centre National de la Recherche Scientifique & Université Pierre et Marie Curie, 2 rue Henry Dunant, 94320 Thiais, France
E-mail: colomban@glvt-cnrs.fr

Non-destructive Raman and Rayleigh microspectrometries were used to map nanostructural and topological variations across the diameter of the SCS-6^{TM} Textron SiC fibre. It is shown for the first time that Rayleigh imaging offers a competitive alternative to AFM measurements for materials containing carbon as a second phase. The Spatial Correlation Model has been used to decompose the SiC Raman spectra into amorphous and crystalline components. 'Smart' Raman images, which contain the calculated structural parameters revealed the nanostructure distribution. A good agreement has been obtained at the nanoscale between these smart images and transmission electron microscopy (TEM) data. A major asset of Raman 'smart' images is to give a non destructive and global view on the crystal quality, grain size and residual stress. The potential and the limitations of the procedure are discussed.

1. Introduction

Nanophased materials received considerable attention in the last few years but their characterisation is not easy. The challenge for the nanotechnologies, which is to achieve perfect control on nanoscale related properties, requires to correlate the production conditions with the resulting nanostructure. Nanocrystalline silicon carbide materials are interesting because of their remarkable properties such as high thermal stability, extreme hardness and good dielectric properties. They are expected to have applications in wide-gap semiconductors, air and spacecraft thermostructural composites, etc. SiC crystallises in a large number of polymorphs made of Si/C bilayers with various stacking combinations called polytypes [1]. Each one has its own band gap energy and electrical properties. Recent development in crystal growth technology such as molecular beam epitaxy or pulsed laser deposition [2] for SiC crystals requires the polytypes structure identification to optimise the material properties. Raman microspectroscopy is a powerful technique for the characterisation of SiC since it is a low-cost (non vacuum) and non-destructive method with a high efficiency because of the strong covalency of Si—C bonds [3]. This method provides information even on heterogeneous materials (e.g., composites), such as the phases nature, distribution, residual stress, etc. [4]. The main advantage compared to infrared spectroscopy is that the laser in Raman equipment can be focused down to $\sim$1 μm, allowing for imaging specific areas [5, 6]. In the case of resonant materials, Raman scattering becomes a surface analysis technique in the range of $\sim$20 to 100 nm in-depth penetration [7].

The purpose of this paper is to show how Raman and Rayleigh microspectrometries can image structural and topological information from heterogeneous materials. As an example, we analysed the SCS-6^{TM} Textron SiC fibre (ϕ = 140 μm), which is prepared by chemical vapour deposition (CVD) of a SiC/C mixture on a C fibre. This fibre finds applications in metal-matrix composites, as reported previously [8–10]. Comparison is made with available data from transmission electron microscopy (TEM). The objective is to image the nanophases physical properties distribution based on an accurate modelling of Raman spectra.

2. Experimental procedure

2.1. Samples

Silicon carbide fibres produced by the chemical vapour deposition (CVD) process are composites in themselves and present structural changes linked to the production

*Author to whom all correspondence should be addressed.

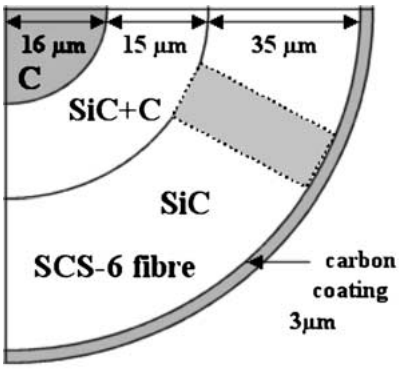

Figure 1 Schematic of the SCS-6 fibre microstructure. The area of the Raman images shown in Figs. 7 and 8 is displayed (dotted lines).

temperatures [11]. The SCS-6 fibre microstructure has already been characterised over the whole fibre diameter. This fibre basically consists of a $\sim$50 μm layer of SiC deposited on a carbon filament of $\sim$33 μm diameter, with a final carbon coating, as is shown in Fig. 1. The only region of the fibre where SiC can be investigated using Raman spectrometry is the 35 μm large 'pure SiC' region (see Fig. 1). In all other regions, SiC signal is indeed more or less masked by the resonant carbon moieties. Ning *et al.* observed by TEM a progressive change of the SiC grain size from about 250 nm in the inner part of the 'pure SiC' region to 90 nm near the fibre surface [11]. This structural change is interesting to evaluate the sensitivity and accuracy of our model and we should focus our Raman measurements on this region. In order to analyse the fibre across its diameter, it was first coated using nickel electro-deposition (thickness $\sim$2 mm) and then polished to the micron using SiC powder plates and 3, 1 and 0.25 μm diamond pastes.

2.2. Raman/Rayleigh microspectrometries

We used a LabRAM "Infinity" (Jobin-Yvon–Horiba, France) Raman micro-spectrometer including Notch filters and equipped for signal detection with a back-illuminated charge coupled device (Spex CCD) cooled by Peltier effect to 200 K. Two different lasers have been used: a He-Ne (632.8 nm, spectral resolution: 2 cm^{-1}) and a doubled frequency Nd:YAG (532 nm, spectral resolution: 3 cm^{-1}).

According to previous experiments, the excitation power was kept at a few milliwatts/μm^2 (measured on the sample), in order to avoid any thermal effect [12, 13]. For the micro-Raman measurements in the backscattering configuration, the laser spot diameter (or waist) was about 1.5 and 3 μm with $\times$100 and $\times$50 long focus Olympus MSPlan objectives (numerical aperture = 0.80 and 0.55) respectively. The total magnification being 1000 and 500; the focal length was 300 mm and the confocal hole aperture was 300 μm. Because of the 'diabolo' shape of the laser convergence along the vertical axis, the in-depth focusing in air covered 4 and 12 μm with $\times$100 and $\times$50 objectives respectively (20–100 nm in resonant materials [7]). Raman cartographies have been performed using a computer controlled XY plate allowing for $\sim 0.1\mu$m displacement steps.

2.3. Peak-fitting procedure

The first step in view of modelling the Raman spectra is to assign the different components to their specific phases and obtain a correlation between the Raman parameters and the physical properties. The decomposition of Raman spectra, which is necessary to get structural parameters, has been performed using the laboratory produced "PARADIS" software based on the Levenberg-Marquardt method [14]. The spectra did not receive any 'manual' treatment since the software automatically sets the baseline in the decomposition (for complex backgrounds we introduced Gaussians). For the decomposition of the SiC Raman peaks we used the spatial correlation model (SCM), which is presented in Section 3 (the whole procedure is summarized in Fig. 2). A reference spectrum is decomposed first (shape and intensity modelling) and the result serves as a starting point for one of the neighbouring spectra. Each spectrum is decomposed using the data coming from its neighbour which minimises the standard deviation when decomposition starts. When the model contains only Gaussians and/or Lorentzians, the calculation is short (a few seconds per spectrum). However, each dissymmetrical peak (shown in Fig. 4) introduced in the model increases the calculation time by a factor 5 or more. A typical decomposition with 10 symmetrical and 3 dissymmetrical peaks takes one minute per spectrum (considering 1000 points in a 1500 cm^{-1} spectral window) on a 1.8 GHz computer. The images of the parameters such as the wavenumber or the peak intensity are finally treated using Origin 5.0 software (MICROCAL^{TM} Software, Inc., USA).

2.4. AFM analysis

Fibre polished sections have been investigated using an AccurexII Atomic Force Microscope (Topometrix Corp. Santa Clara, CA, USA). AFM images were treated using the SPMLab NT 5.0 (Topometrix) software. The background levelling has been performed with a planar correction, assuming that each point of the fibre periphery was at the same level.

3. SiC structure and Raman scattering

SiC structures alternate layers of Si and C atoms. Two consecutive layers form a bilayer which is named "h" if it is deduced from the one below by a simple translation. If not, when an additional 180° rotation (around the Si–C bond linking the bilayers) is necessary to get the superposition, then the bilayer is named "*k*" [15]. The "*k*" only stacking is the reference β-SiC structure, of cubic symmetry. Its main Raman peaks are centred at 796 and 972 cm^{-1} and correspond to the transverse (TO) and longitudinal (LO) optic modes, respectively [16]. Any other definite stacking sequence is called α-SiC and has either hexagonal or rhombohedral lattice symmetry, depending on the relative position of the stacked bilayers (shift and/or rotation).

3.1. The spatial correlation model (SCM)

In "large" crystals, phonons propagate "to infinity" and the first order Raman spectrum only consists of "$q = 0$"

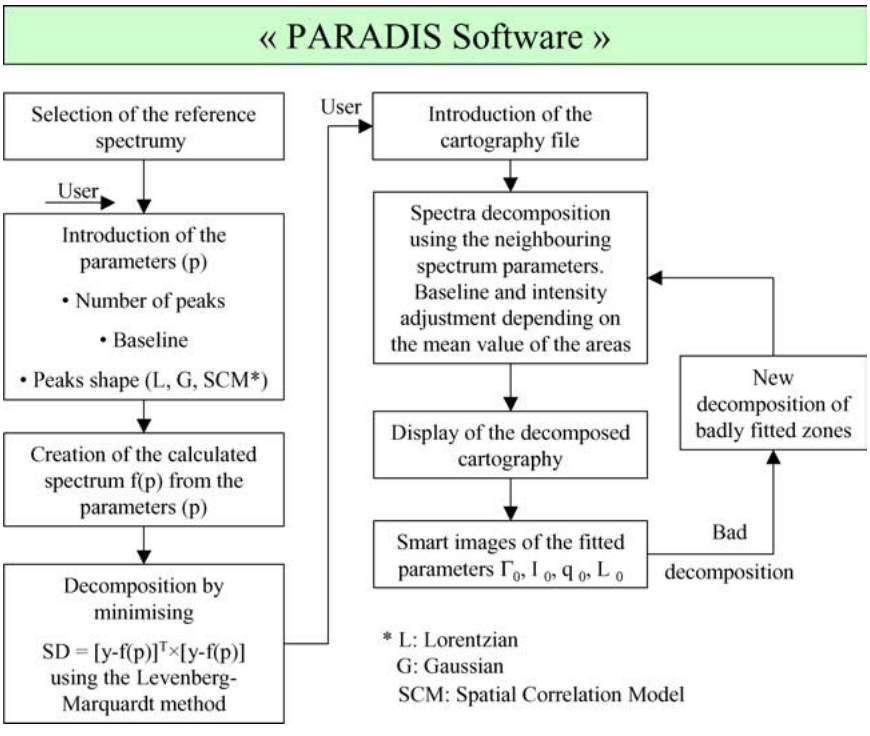

Figure 2 Scheme of the decomposition procedure using the laboratory made "PARADIS" software (SD = Standard Deviation; Γ_0, I_0, q_0 and L_0: see text for definitions).

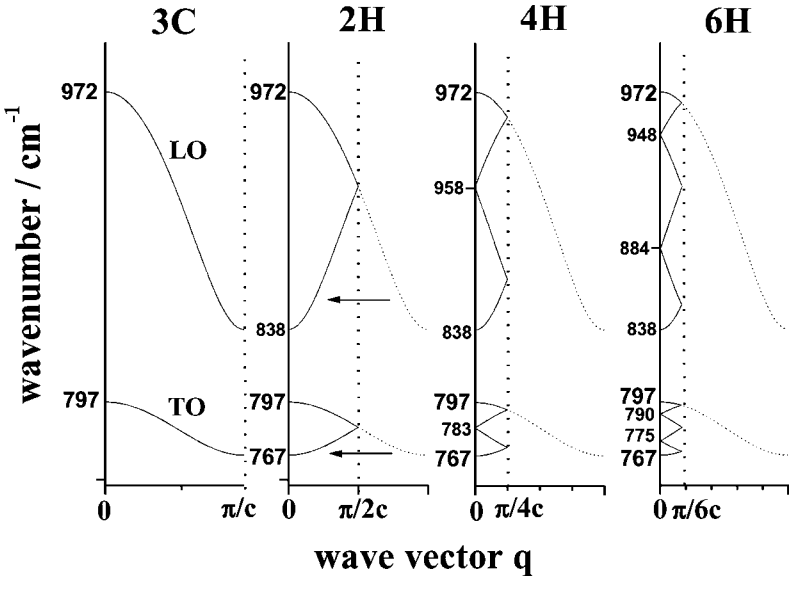

Figure 3 Schematic of the relationship between the 3C structure and the polytypes obtained by folding the Brillouin zone 1, 2 or 3 times along the *c*-axis, in the stretching region. The Raman active modes are located at $q = 0$.

phonon modes (momentum selection rule). However, since crystalline perfection is destroyed by impurities or lattice disorder, including at the surface where atoms environment is singular, the phonon function of polycrystals is spatially confined [17, 18]. This results in an exploration of the wavevectors space and subsequent wavenumber shifts and band broadening. Another effect is the possible activation of "symmetry forbidden" modes. This is linked to the Brillouin zone folding as is illustrated in Fig. 3. In the 6H polytype structure, the zone is folded three times at the Γ point and the reduced wave vectors that can be observed are at $q = 0$, 0.33, 0.67 and 1. The Raman line broadening can be described by the (linear) dependence of its half width upon the inverse grain size, as reported previously for many nanocrystalline materials including CeO_2 [19, 20], BN [17], Si [18], Ge [21], . . .

The SCM describes the crystalline quality by introducing a parameter L_0, the coherence length, which is the average extension of the material homogeneity region. Noting q the wave vector expressed in units of π/a (a being the lattice constant) and Γ_0 the half width of Raman peaks for the ordered reference structure, the intensity $I(\bar{\nu})$ at the wavenumber $\bar{\nu}$ is then given by (1) [17, 18]. The exponential function represents a Gaussian spatial correlation and $\bar{\nu}(q)$ is the mode dispersion function, which can be deduced from neutron scattering measurements or from calculations often based on

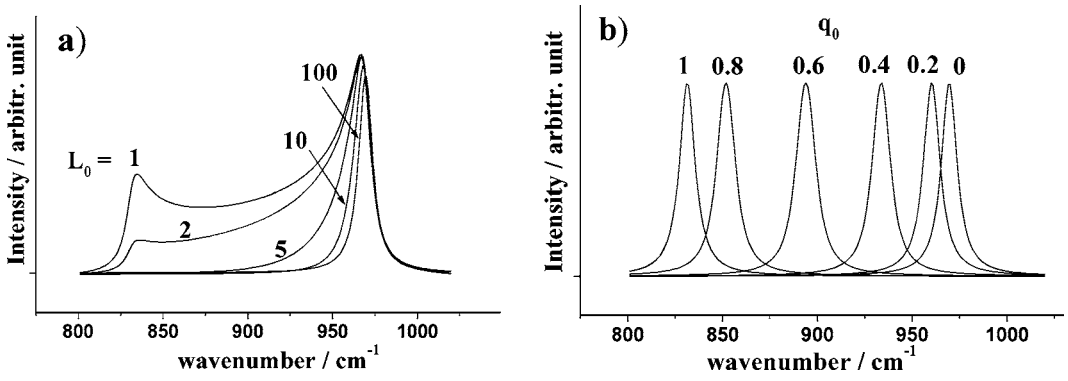

Figure 4 Variations of LO mode shape predicted by the SCM: (a) L_0, changes at q_0 and Γ_0 fixed at 0 and 10 cm^{-1} respectively and (b) q_0, changes at L_0 and Γ_0 fixed at 100 nm and 10 cm^{-1} respectively.

a rigid-model structure [19, 20, 22, 23]. In the specific case of SiC, the data collected from the different polytypes allow to built part of the dispersion curve.

$$I(\bar{\nu}) = I_0 \times \int_{q=0}^{q=1} e^{-\frac{k_{BZ}^2 \times (q-q_0)^2 \times L_0^2}{16 \times \pi^2}} \times \frac{\mathrm{d}q}{[\bar{\nu} - \bar{\nu}(q)]^2 + \left(\frac{\Gamma_0}{2}\right)^2} \quad (1)$$

Fig. 4 illustrates the evolutions of the LO mode as a function of the q_0 and L_0 parameters i.e., of the disorder. While the one dimensional disorder (in the stacking direction) leads to the polytypes formation, a complete disorder induces the total folding of the Brillouin zone and the apparition of a very broad Raman signal (density of state spectrum). The phonon confinement is observed for small grains in a well crystallised state.

The dispersion curve has to be known with a high accuracy to calculate Equation 1. It can be modelled with the expressions (2–4), introduced by Parayanthal and Pollak [23]. Equation 2 depends on the peak positions at $q = 0$ and 1 only. Considering the TO mode of the 6H structure, the literature gives the following values: 797-767 [3], 794-766 [24] and 797-769 [25]. The slight differences can be related to the instrument accuracy, ± 1 cm^{-1} typically. Our 6H reference corresponds to the first set of values and the resulting A and B coefficients, that have been used in our model [26], are reported in Table I.

$$\bar{\nu}(q) = \sqrt{A + \sqrt{A^2 - B \times (1 - \cos(\pi q)}} \quad 0 \leq q \leq 1 \quad (2)$$

$$\text{with } A = \frac{1}{2} \times \bar{\nu}_{(q=0)}^2 \quad (3)$$

TABLE I Coefficients selected to fit the 6H-SiC dispersion curve in the ΓL direction of the Brillouin zone

	TO mode	LO mode
Coefficient A	3.18×10^5	4.72×10^5
Coefficient B	1.38×10^{10}	8.52×10^{10}

and

$$B = \frac{1}{2} \times \bar{\nu}_{(q=1)}^2 \times \left(\bar{\nu}_{(q=0)}^2 - \bar{\nu}_{(q=1)}^2\right) \quad (4)$$

4. Results and discussion

4.1. Rayleigh imaging: A topological analysis

The interaction of light with matter can be either elastic or inelastic, giving rise in the visible range to Rayleigh and Raman scattering respectively. The former has been evidenced by Lord Rayleigh in 1871 [27]. In any system, the spectrum of scattered light is proportional to the Fourier transform (in space and time) of the dielectric constant correlation function, as is shown in Equation 5 [28].

$$I(\overrightarrow{k}, \omega) = \frac{I_0 k_i^4}{16\pi^2 r^2} \times V^2 \times S(\overrightarrow{k}, \omega) \quad (5)$$

where I_0 is the intensity of the incident light, V is the scattering volume, r is the distance from the scattering region to the point of observation, ω is the frequency change of the scattered light, $\overrightarrow{k}$ is the difference between the final and incident wave vectors of the scattered light and S is the dielectric correlation function (k_i is the magnitude of the incident light wave vector).

It appears that Rayleigh scattering is a function of the interacting matter volume and of the optical properties of materials. However, when the analysed material presents a constant dielectric function, the information is mainly topological. When performed using a laser beam focused with a microscope, Rayleigh scattering allows to image topological and/or optical information of materials with a near micron resolution [13]. Indeed, thanks to the high Rayleigh scattering efficiency ($\times 10^6$ compared to Raman scattering), it becomes possible to make surface mappings very quickly [13]. A condition to do such experiments is that an absorbing (Raman resonant) phase be present as a second phase in the material, to limit light penetration. This is the case in the SCS-6 fibre. Fig. 5 shows two micrographs of the SCS-6 cross section obtained by AFM and Rayleigh imaging and the corresponding profiles (linescans). AFM evidences a carbon core level higher than for the rest of the fibre, whereas Rayleigh imaging indicates a lower signal level. This is linked to the strong absorption of

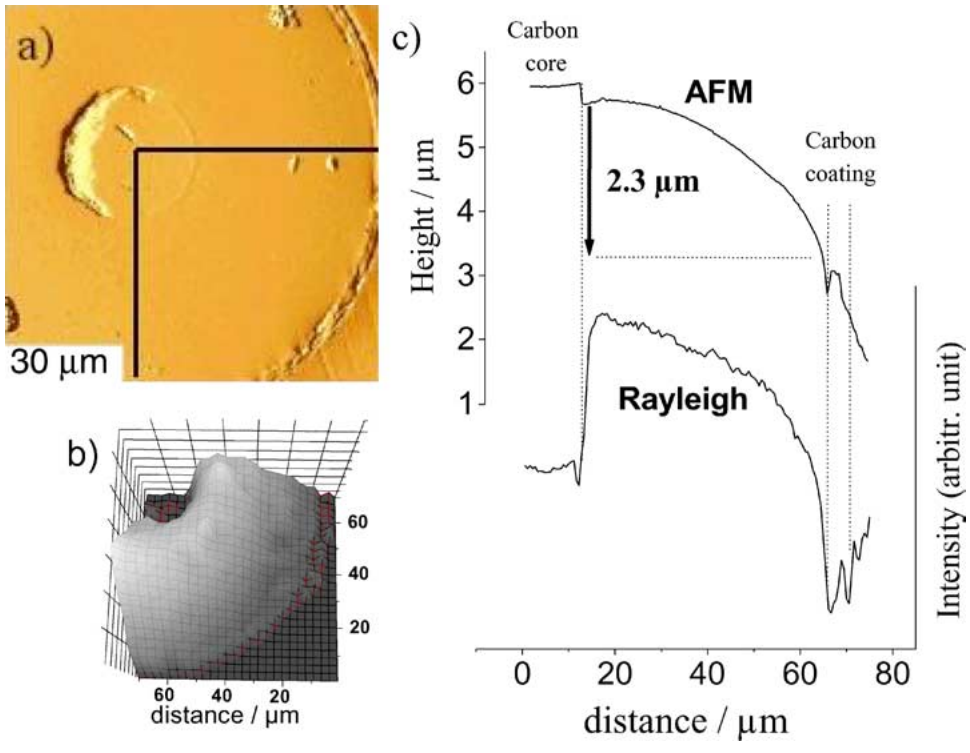

Figure 5 (a) AFM micrograph showing the SCS-6 fibre cross section geometry (300 × 300 dots recorded in 1 h, with 0.3 μm step). The quarter analysed in (b) is highlighted; (b) Rayleigh image of the SCS-6 fibre quarter. (26 × 26 spectra recorded in 15 min, with 3 μm step, objective ×50); (c) height profiles across the fibre section from the core (0 μm) to the surface (70 μm) obtained by AFM and Rayleigh imaging.

the light by the carbon phase. In the region from 16 to 66 μm, the Rayleigh and AFM profiles are in good agreement: both indicate a height decrease from the core to the surface. This profile is due to a polishing effect.

Then, in the case of SiC/C materials, Rayleigh imaging can be used to evaluate the surface geometry. This approach is very interesting since two consecutive Rayleigh and Raman images can be performed without moving the sample. Indeed, associating AFM and Raman imaging makes it hard to locate precisely a specific area (corrosion figure, indentation stamp, chemical interface, etc.). Combining Raman and Rayleigh imaging allows to obtain chemical and topological information in a very competitive time (few minutes for linescans and less than an hour for two dimensional images, depending on the resolution) when compared to the AFM method.

4.2. Raman imaging: A nanostructural analysis

4.2.1. Raman peaks assignment

Fig. 6 shows the Raman spectra recorded in the inner and outer part of the 'pure SiC' region. They are displayed with their decomposition, which considers two nanophases: the crystalline and the amorphous SiC.

– In crystalline SiC, Raman signature consists of sharp peaks. Their position and shape are related to the SiC structure, allowing for the polytypes identification. In Fig. 6 the only two sharp peaks are centred at ~795 and 767 cm^{-1} corresponding to the TO mode of the 6H polytype.

– In amorphous SiC, the best modelling is obtained with Gaussians, indicating a broad isotropic distribution of bond length and angles. That is why we assigned the two broad Gaussian peaks at ca. 894

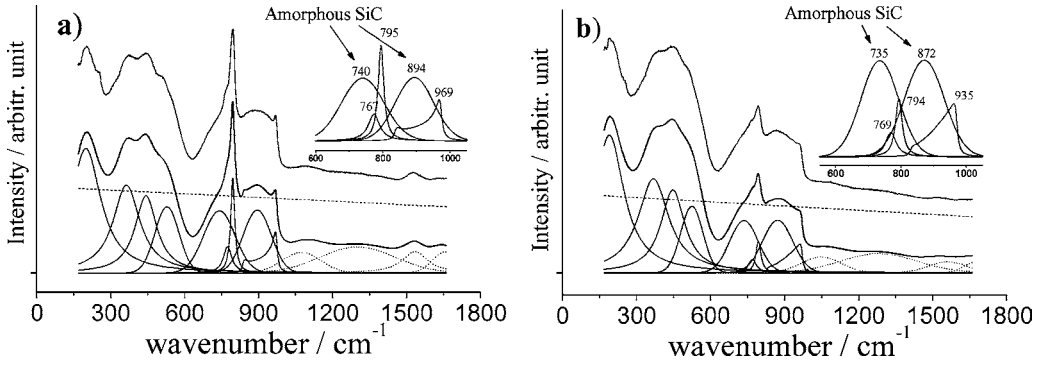

Figure 6 Raman spectra of the inner (a) and outer (b) part of the 'pure SiC' region of the SCS-6 fibre (λ = 632 nm, 1 mW, 200 s). The decomposition using the SCM is shown.

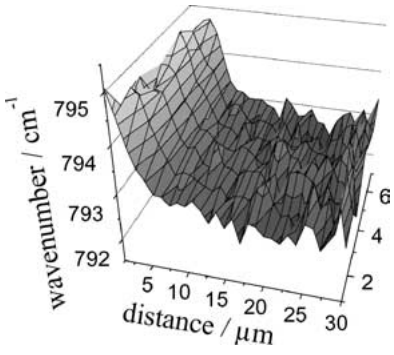

Figure 7 Raman image of the wavenumber variations of the TO mode across the 'pure SiC' region (30 × 7 spectra, 150 s per spectrum, 0.5 mW, 632 nm).

and 740 cm^{-1} to the amorphous phase. Furthermore, the position of the band at ca. 894 cm^{-1}, between the two optical modes and at a wavenumber close to $(795 + 969)/2 = 882$ cm^{-1}, allows us to assign it to non-polar SiC, as expected for an amorphous phase. Finally, the band at ca. 740 cm^{-1} has already been assigned to the amorphous phase by Dkaki *et al.* [29], who used infrared absorbance (but no IR/Raman exclusion occurs in amorphous compounds) to investigate the crystallisation process of silicon-carbon alloys.

4.2.2. Raman cartographies

In order to point out the structural changes across the diameter (crystalline fraction, grain size and stacking faults) we performed two dimensional 30 × 7 spectra Raman scans, in the 'pure SiC' region shown in Fig. 1 (35 × 7 μm). The direct mapping of Raman parameters is hereafter called 'Raman imaging' whereas the mapping of physical parameters calculated from Raman measurements through a model is called 'smart imaging'.

4.2.3. Raman imaging

Fig. 7 shows the wavenumber variations of the TO mode at $\sim$ 795 cm^{-1}. We observe a decrease from 795 cm^{-1} near the SiC+C/pure SiC boundary to 792 cm^{-1} near the fibre surface. Olego *et al.* [30] observed a strong dependence of this mode (measured on 3C-SiC) on pressure of 3.88 ± 0.08 cm^{-1}/GPa. It appears that SiC grains are in compression at the beginning of the 'pure SiC' CVD process and that this stress is then slightly relaxed as the deposition progresses.

4.2.4. Smart imaging

Fig. 8 shows the variations of three calculated parameters: the wave vector q_0 giving information on the crystal quality, the coherent length L_0 which is correlated to the size of the nanograins (here SiC) and the crystalline fraction which is calculated from the area ratio of the two Raman peaks at ca. 793 and 723 cm^{-1}. The q_0 parameter is submitted to drastic changes across the fibre. Indeed, it strongly decreases during the first 10 μm and then increases before reaching a plateau at $q_0 = 0.45$. These changes are linked to the SiC stacking sequences in the k direction and hence to the crystal quality. We can assume that at the beginning of the 'pure SiC' CVD procedure, the deposited SiC is hardly faulted due to the growth conditions onto the SiC+C substrate ($q_0 = 0.7$) and then stabilises over $\sim$10 μm until q_0 reaches 0.2. After that, a change in the CVD conditions may have stabilised a SiC polytype corresponding to the wavevector $q_0 = 0.45$.

The variations of L_0 indicate a constant size during the first 10 μm and a strong increase after, from 1.5 to 4 nm. This is consistent with the change in the growth conditions that we assumed previously regarding the q_0 variations. Note that the calculated size is linked to the homogeneous vibrationnal units and not to the real grain size. However, a relative comparison remains possible.

The crystal fraction is also constant at the beginning and then slightly decreases towards the fibre surface. The extinction of the crystalline SiC Raman signal, which is not consistent with the grain size increase indicated by L_0 variations, may be due to a scattering efficiency decrease. Indeed, the scattering efficiency depends on the SiC structure [7] which changes across the diameter.

4.3. Comparison to TEM data

Ning *et al.*, who carried a TEM investigation of the SCS-6 fibre [11] found no sharp transition in the region at 10 μm from the SiC+C/'pureSiC' boundary. They rather observed a progressive change in the size

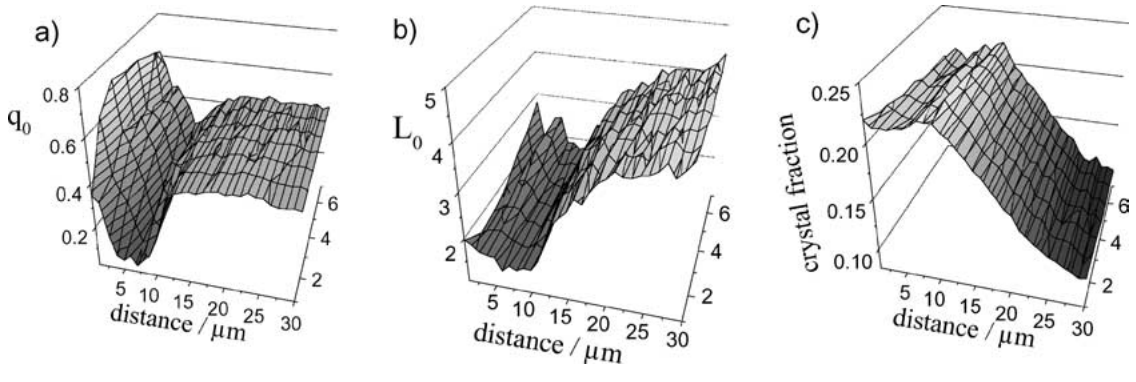

Figure 8 Smart images across the 'pure SiC' region of (a) q_0 parameter; (b) L_0 parameter and (c) the crystalline fraction calculated from the area ratio of the two peaks at ca. 793 and 723 cm^{-1}. (30 × 7 spectra, 150 s per spectrum, 0.5 mW, 632 nm).

of the SiC grains from about 250 nm in the inner part to 90 nm near the fibre surface. They concluded that the temperature was gradually decreased during the CVD procedure, giving rise to smaller grains and lower stress concentrations. Our results also indicate a stress relaxation, as is shown in Fig. 7, but are not in agreement regarding the grain size (which we found to increase (Fig. 8)). To explain this difference between MET and Raman measurements, our results have to be interpreted regarding the short range nanostructure rather than the microstructure observed by MET. Indeed, if we look at the high resolution TEM micrographs obtained by Ning *et al.* [11], we observe a nanocrystalline structure with homogeneous SiC domains between 1 and 10 nm in size. This size range is consistent with the one calculated from our Raman measurements.

4.4. Limitations of the procedure

4.4.1. The spatial correlation model

First of all, the SCM requires a high accuracy on the wavenumber ($\sim$1 cm^{-1}) both on the spectrum and dispersion curve. Another sensitive point is the quality of the decomposition, which mainly depends on the number of peaks chosen to fit the background and on the baseline. The impact of the latter is reduced since the baseline is introduced in the decomposition. In addition, for a given structure, there are as many dispersion curves as high symmetry points (Γ, L, X, etc.) and they may modify the Raman signal with an unknown weight. Finally, we assume that there is no residual stress in the sample, which is a questionnable approximation for nanophased materials.

4.4.2. Raman and Rayleigh imaging

The potential of Rayleigh imaging to get topological information has been demonstrated. However, the in-depth laser penetration has to be low (a few tens of nanometers) which should limit investigations to opaque materials. The problem of the spatial resolution obtained in our images ($\sim$3 μm) is linked to the width of the laser spot ($\phi \sim 3$ μm with a $\times$50 objective). The deconvolution of the image by the spot shape, which could increase the final resolution, is in progress. However, the ultimate resolution cannot be lower than the convolution of the laser exciting wavelength ($\sim$ 0.5 μm) by the displacement step of the sample using an XY plate ($\sim$0.1 μm).

5. Conclusion

For a few years, Raman imaging has been achieved in some materials. In this study, Rayleigh and Raman mappings were combined to provide topological and structural information at once on an SCS-6^{TM} fibre cross section. It is demonstrated that Rayleigh imaging offers a good alternative to AFM measurements for materials containing a coloured second phase (e.g., carbon). Raman spectra were decomposed using the spatial correlation model and the calculated structural parameters were mapped, providing 'smart' images. These images are consistent with that obtained from TEM: the crystal quality and the grain size variations indicate strong changes in the production conditions. Furthermore, a progressive stress relaxation has been pointed out from the SiC+C/pure SiC boundary to the fibre's surface. Then, Raman imaging appears to be an efficient and non-destructive tool to map structural variations in heterogeneous materials. It could probably be used along the process of materials manufacture. This procedure can be applied to other systems, provided a good understanding of the Raman spectra.

Acknowledgements

The authors would like to thank Mrs M.-H. Ritti (ONERA, Department of Composite Materials and Systems) for performing AFM images and Dr. G. Gouadec for many fruitful discussions.

References

1. F. BECHSTEDT, P. KÄCKELL, A. ZYWIETZ, K. KARCH, B. ADOLPH, K. TENELSEN and J. FURTHMÜLLER, *Phys. Stat. Sol.* (b) **202** (1997) 35.
2. H. HOBERT, H. H. DUNKEN, S. URBAN, F. FALK and H. STAFAST, *Vibrational Spectrosc.* **29** (2002) 177.
3. S. NAKASHIMA and H. HARIMA, *Phys. Stat. Sol.* **162** (1997) 39.
4. R. J. YOUNG, *J. Microscopy* **185** (1996) 199.
5. J. WINDELN, C. BRAM, H. L. ECKES, D. HAMMEL, J. HUTH, J. MARIEN, H. RÖHL, C. SCHUG, M. WAHL and A. WIENSS, *Appl. Surf. Sci.* **179** (2001) 167.
6. PH. COLOMBAN and M. HAVEL, *J. Raman Spectrosc.* **33** (2002) 789.
7. PH. COLOMBAN, G. GOUADEC and L. MAZEROLLES, *Mater. Corrosion* **53** (2002) 306.
8. B. GUICHET, J. C. SANGLEBOEUF, A. VASSEL and T. BRETHEAU, *Comp. Sci. Tech.* **58** (1998) 665.
9. S. R. NUTT and F. E. WAWNER, *J. Mater. Sci.* **20** (1985) 1953.
10. M. LANCIN, J. THIBAULT-DESSEAUX and J. S. BOUR, *J. Microsc. Spectrosc. Electron.* **13** (1988) 503.
11. X. J. NING and P. PIROUZ, *J. Mater. Sci.* **6** (1991) 2234.
12. G. GOUADEC and PH. COLOMBAN, *J. Eur. Ceram. Soc.* **21** (2001) 1249.
13. M. HAVEL and PH. COLOMBAN, in Proceedings of the 105th Annual American Ceramic Society Conference and Exposition, edited by N. Bansal (Ceramics Transaction, Nashville, 2003).
14. K. LEVENBERG, *Qu. Appl. Math.* **2** (1944) 164.
15. W. J. CHOYKE and G. PENSL, *MRS Bull.* **22** (1997) 25.
16. H. OKUMURA, E. SAKUMA, J. H. LEE, H. MULKAIDA, S. MISAWA, K. ENDO and S. YOSHIDA, *J. Appl. Phys.* **61** (1987) 1134.
17. R. J. NEMANICH, S. A. SOLIN and R. M. MARTIN, *Phys. Rev.* B **23** (1981) 6348.
18. H. RICHTER, Z. P. WANG and L. LEY, *Solid State Commun.* **39** (1981) 625.
19. I. KOSACKI, T. SUZUKI, V. PETROVSKY, H. U. ANDERSON and PH. COLOMBAN, *Solid State Ionics* **149** (2002) 99.
20. W. H. WEBER, K. C. HASS and J. R. MCBRIDE, *Phys. Rev.* B **48** (1993) 178.
21. M. FUJII, S. HAYASHI and K. YAMAMOTO, *J. Appl. Phys.* **30** (1991) 687.
22. I. KOSACKI, V. PETROVSKY, H. U. ANDERSON and PH. COLOMBAN, *J. Amer. Ceram. Soc.* **85** (2002) 2646.
23. P. PARAYANTHAL and F. H. POLLAK, *Phys. Rev. Lett.* **52** (1984) 1822.
24. D. W. FELDMAN, J. H. PARKER, W. J. CHOYKE and L. PATRICK, *Phys. Rev.* **170** (1967) 698.

25. M. HOFMANN, A. ZYWIETZ, K. KARCH and F. BECHSTEDT, *ibid* B **50** (1994) 13401.
26. G. GOUADEC, "Analyse (micro)-mécanique et (nano)-structurale des solides hétérogènes par spectroscopie Raman," thesis, University of Rennes 2001, Vol 1.
27. J. W. STRUTT (later Lord RAYLEIGH), *Phil. Mag.* **41** (1871) 107.
28. C. COHEN, P. D. FLEMING and J. H. GIBBS, *Phys. Rev. B* **13** (1976) 866.
29. M. DKAKI, L. CALCAGNO, A. M. MAKTHARI and V. RAINERI, *Mater. Sci. Semicond. Proc.* **4** (2001) 201.
30. D. OLEGO and M. CARDONA, *Phys. Rev.* B **25** (1982) 3878.

Received 3 December 2003
and accepted 3 June 2004